Quantitative Characterization of Inertial Confinement Fusion Capsules Using Phase Contrast Enhanced X-Ray Imaging

B. J. Kozioziemski, J. A. Koch, A. Barty, H. E. Martz, W-K. Lee, K. Fezzaa

July 1, 2004

Disclaimer

Quantitative characterization of inertial confinement fusion capsules using phase contrast enhanced x-ray imaging

B. J. Kozioziemski, J. A. Koch, A. Barty, and H. E. Martz Jr.

Lawrence Livermore National Laboratory, Livermore CA 94551

Wah-Keat Lee and Kamel Fezzaa

Advanced Photon Source, Argonne National Laboratory, 9700 South Cass Avenue, Argonne, IL 60439

Current designs for inertial confinement fusion capsules for the National Ignition Facility (NIF) consist of a solid deuterium-tritium (D-T) fuel layer inside of a copper doped beryllium, Be(Cu), shell. Phase contrast enhanced x-ray imaging is shown to render the D-T layer visible inside the Be(Cu) shell. Phase contrast imaging is experimentally demonstrated for several surrogate capsules and validates computational models. Polyimide and low density divinyl benzene foam shells were imaged at the Advanced Photon Source synchrotron. The surrogates demonstrate that phase contrast enhanced imaging provides a method to characterize surfaces when absorption imaging cannot be used. Our computational models demonstrate that a rough surface can be accurately characterized using phase contrast enhanced x-ray images.

I. INTRODUCTION

Indirect drive inertial confinement fusion (ICF) experiments, such as those planned at the National Ignition Facility (NIF), use x-ray ablation to compress a spherical fuel layer to high density.[1–3] Rayleigh-Taylor instabilities seeded by rough ablator or fuel layers can prevent ignition and burn of the fuel layer.[4, 5] Current specifications require less than 1 μm root-mean-squared (RMS) roughness for the 1 mm radius ablator and fuel layers.[6, 7] Thus, careful preparation and characterization of both the ablator and fuel are required to ensure ignition.

Solid deuterium-tritium (D-T) mixtures, in a 50-50 ratio, approximately 100 μm thick will be used as the fuel layer for ignition experiments at the NIF. Several ablator materials are currently under consideration. A beryllium ablator with graded copper doping, Be(Cu), is one choice that is very stable against Rayleigh-Taylor growth.[8, 9] The D-T layer inside of the Be(Cu) ablator cannot be characterized using visible light. Ultrasonic methods for characterization of the D-T layer have the potential to measure the D-T fill, but have not yet proved successful for characterization of the solid.[10–12] While x-ray absorption measurements are suitable for characterizing the Be(Cu) ablator, hydrogen and its isotopes weakly absorb x-rays with energies required for sufficient penetration through the Be(Cu) ablator. Phase-contrast enhanced x-ray imaging has been proven for low atomic number materials and should enable characterization of the D-T fuel layers.

Phase-contrast enhanced imaging describes a variety of methods for obtaining contrast from objects with very little absorption.[13, 14] Interferometry,[15–19] diffraction-enhanced imaging,[20, 21] and in-line holography[22] are some of the currently employed techniques for phase-enhanced imaging. Characterization of laser fusion shells using x-ray interferometry was pro-posed many years ago.[23] Similarly, a double-crystal diffractometer was described for characterizing the shell wall thickness.[24] Interferometric methods require very sensitive interferometers and extremely stable environments. Non-interferometric methods have recently been demonstrated and have the advantage of relaxed requirements on sample environment and spatial and temporal coherence.[25–30] Successful imaging using a commercially available table-top micro-focus x-ray tube has been demonstrated.[31, 32] The size and required resolution for characterizing NIF D-T fuel layers makes non-interferometric imaging suitable for D-T layers inside of Be(Cu) ablators. Calculations for such imaging of D-T layers has recently been carried out.[33]

This paper describes proof-of-principle experiments at the Argonne National Laboratory Advanced Photon Source (APS) demonstrating phase-contrast enhanced x-ray imaging for surrogates of D-T layers inside of Be(Cu) ablators. For this paper, the NIF baseline fuel capsule design is taken to be a spherical shell of beryllium with uniform copper doping of 1 atom percent that has a 1.0 mm outer radius and a 150 μm wall thickness. The Be(Cu) shell surrounds a 100 μm thick spherical shell of solid D-T. The center region of the capsule is filled with the low density D-T vapor consistent with the vapor pressure of solid D-T. Surrogate materials were chosen to eliminate the need for cryogenic and tritium handling capabilities in these first tests. Raytracing models show good agreement with the experimental data for the surrogates and provide confidence that D-T can be imaged inside of Be(Cu) ablator shells. Accurate characterization of a rough layer using phase-contrast enhanced imaging is demonstrated using raytracing models.

II. PHASE CONTRAST IMAGING

A. Refractive indices of D-T and Be(Cu)

The complex refractive index of a material is expressed as $n = (1 - \delta) + i\beta$ when operating in the x-ray wavelength regime. The phase shift is proportional to the real part, δ, while the absorption is proportional to the imaginary part, β. In radiography terminology, the absorption length $\mu = 2\pi\beta/\lambda$, where λ is the wavelength. Both δ and β are functions of the x-ray energy. Absorption radiography is appropriate when $1 \leq \mu l \leq 3$,[34] where l is the path length through the object under study. For x-ray energies > 1 keV, μ is several thousand times larger for Be(Cu) than for D-T. Thus, there is no x-ray energy where Be(Cu) and D-T can be simultaneously characterized by absorption imaging.

Since absorption imaging cannot be used to characterize D-T inside of Be(Cu), the x-ray energy needs to be optimized for phase contrast enhanced imaging. The goal is to maximize δ for solid D-T while minimizing the x-ray absorption through the Be(Cu) shell. The maximum path length through the Be(Cu) shell for the baseline NIF capsule is 1054 μm. Combining this with β for Be(Cu) to calculate the x-ray transmission, a low energy peak transmission of 55% occurs just before the Cu K-β line of 8.9 keV. For x-ray energies lower than 8.9 keV, the transmission drops rapidly with decreasing photon energy, reaching 10% at 5.5 keV and 1% at 4.3 keV. The x-ray transmission for photon energies greater than 18 keV is greater than that at 8.9 keV, however δ is reduced by a factor of 4 at 18 keV compared to 8.9 keV. Thus, photon energies near 8 keV are ideal for imaging solid D-T inside of Be(Cu) shells.

TABLE I: Complex refractive indices for the baseline capsule and surrogate materials.[35] The 8 keV x-ray energy is used as a reference for imaging D-T inside Be(Cu) shells, while 10 keV and 20 keV were appropriate for the surrogate materials.

Material	Density (g/cm^3)	x-ray energy (keV)	δ ($\times 10^{-6}$)	β ($\times 10^{-9}$)
D-T (solid)[a]	0.252	8.0	0.65	0.00074
D-T (gas)	0.0006	8.0	0.0016	1.8×10^{-6}
Be(Cu)	1.96	8.0	5.6	10.5
Polyimide	1.43	10.0	3.0	4.0
Polyimide	1.43	20.0	0.76	0.20
CH (plastic)	1.0	10.0	2.2	1.8
CH (plastic)	1.0	20.0	0.56	0.093
DVB (foam)	0.1	10.0	0.22	0.18
DVB (foam)	0.1	20.0	0.056	0.0093

[a]Extrapolated based on H_2 at 0.101 g/cm^3.

Table I lists values of δ and β for D-T and Be(Cu) at 8 keV photon energy. There has been no direct measurement of δ and β for D-T. Since δ and β are proportional to the electron number density, the D-T values can be extrapolated from those of hydrogen (H_2) based on their relative number densities. The values in Table I are those for the mass density of H_2 using the solid D-T triple point number density of 0.0503 moles/cm^3.[36] The mass density of H_2 is 0.101 g/cm^3 at 0.0503 moles/cm^3, a factor of 2.5 less than that of solid D-T.

Copper doping at 1 atomic percent substitutionally replaces the beryllium atoms in the lattice. The number density is assumed to be identical to pure Be for the purpose of calculation. Thus Be with 1 atomic percent of Cu has a density of 1.96 g/cm^3. This density is used to obtain δ and β for the ablator. Inspection of Table I reveals that the absorption constant β for solid D-T is four orders of magnitude lower than for Be(Cu). It is this extreme difference between the absorption coefficients that prevents absorption imaging of D-T inside the Be(Cu) ablator. However, the phase constant δ is only 8.6 times larger in Be(Cu) than for solid D-T.

An electromagnetic wave has both its amplitude and phase changed by passing through an object. Figure 1 shows the amplitude (left) and phase shift (right) relative to vacuum after an 8 keV plane-wave of unit amplitude has passed through a NIF baseline capsule. Note how the amplitude immediately after the object is dominated by absorption of the Be(Cu) shell with little contrast at the inner solid D-T surface. However, the phase shift shows a sharp change at the inner solid D-T boundary. It is this structure in the phase of the wave field exiting the capsule that suggests the inner D-T surface may be rendered visible using phase-contrast imaging.
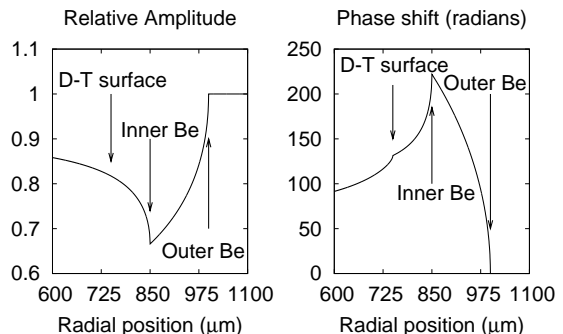

FIG. 1: Calculated amplitude (left) and phase shift (right) introduced on a plane-wave of 8 keV x-rays through the NIF baseline capsule. Note how the amplitude is dominated by absorption of the Be(Cu) shell with little contrast at the inner solid D-T surface, whereas the phase profile shows a sharp change in phase at the inner D-T surface.

Unlike the absorption profile of an object, which can be directly measured, the phase structure can not be directly detected and must be rendered visible using one of many phase contrast imaging techniques. One of the simplest phase contrast microscopy techniques is free-space propagation in which the wave amplitude and phase exiting the object is allowed to propagate through free space.[31, 32]

The resulting image corresponds to the Laplacian of the phase and therefore detects edges in the object.[27, 29] This form of phase contrast imaging is demonstrated for characterizing the solid D-T layer in the NIF baseline capsule by modeling the detected image of a plane-wave incident on the NIF baseline capsule. In this case, the field exiting the capsule has the amplitude and phase shift illustrated in Fig. 1. Wave-based propagation is then used to determine the field at detector planes a distance Δz from the center-plane as shown in Fig. 2.
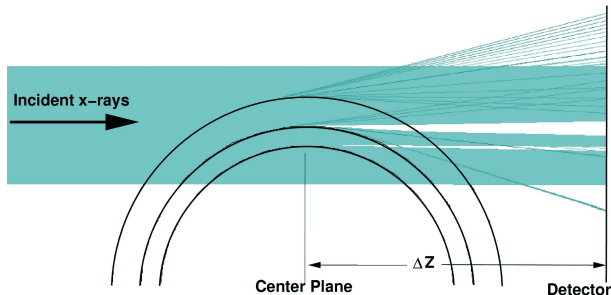

FIG. 2: The x-rays are shown in blue traveling left to right, initially in a collimated band. Strong refraction and diffraction (exaggerated for display) occurs when the x-rays pass tangent to an interface. The wave exiting the capsule is propagated to the detector at distance Δz from the center-plane of the capsule. The displaced x-rays provide image contrast.

Sharp changes in δ and β at edges leads to both refraction and diffraction. Figure 2 shows an exaggerated view of refraction and diffraction due to two concentric shells. Image contrast results from the strong deflection of x-rays passing nearly tangent to the interfaces at the center plane of the shell. Figure 3 shows the evolution of phase contrast as the propagation distance is increased for an 8 keV plane-wave source and a realistic detector pitch of 3 μm. Note that the contrast at the inner D-T surface increases as the propagation distance, Δz, is increased. It is therefore possible to increase contrast of the D-T surface by simply increasing Δz. It is this effect that forms the basis of our characterization technique. The interfaces at the center-plane of the capsule are thus characterized by following the corresponding edges in the phase-contrast enhanced images.

B. Surrogate materials

As a way of emulating planned experiments using D-T layers in Be(Cu) ablator shells, surrogate materials were used to demonstrate the feasibility of phase-contrast enhanced x-ray imaging for hydrogen. An ideal surrogate would have both δ and β comparable to D-T. Unfortunately, no solid material has δ close to the value for D-T at the same photon energy. There are two ways to make δ comparable to that of 8 keV D-T value. The first is to use a low density foam. The second is to use a solid material at higher x-ray energies. Two capsules were obtained
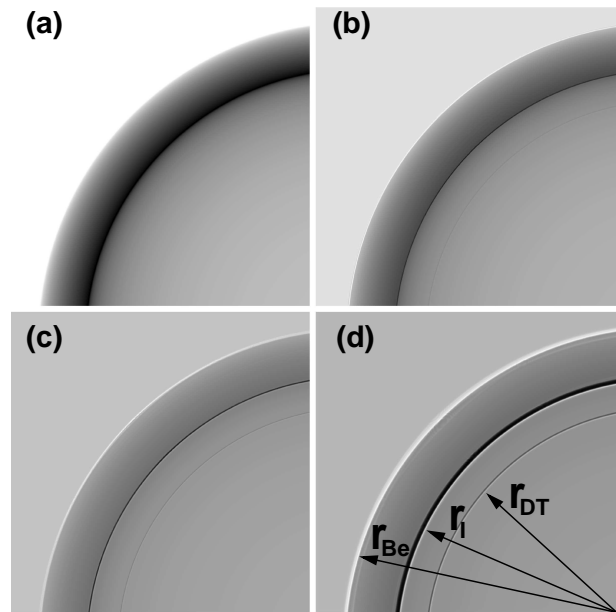

FIG. 3: Images of 1/4 of the NIF baseline capsule from a full-wave calculation of free-space propagation showing the evolution of phase contrast as Δz is increased. The NIF baseline capsule described in the text is illuminated with 8 keV plane-waves, and the calculated image collected at Δz of (a) 2 mm, (b) 7 mm, (c) 22 mm, and (d) 102 mm is shown for a detector with 3 μm detector pitch. The outer Be surface (r_{Be}), inner solid D-T (r_{DT}) and the interface between the Be and solid D-T (r_I) are indicated in (d). Note how contrast at the inner D-T surface is increased by increasing the propagation distance.

so that each method could be tested.

Divinyl benzene (DVB) foams shells have been successfully fabricated with a wide range of densities.[37] DVB was chosen because its chemical composition is only carbon and hydrogen, which both have relatively low x-ray absorption, and because hollow DVB foam shells were readily available. The DVB foam density of 0.1 g/cm^3 was chosen so that the average δ at 10 keV was close to D-T at 8 keV. This assumes that the foam can be modeled simply as a solid material using its average density. This is likely a good approximation since the foam cell size is on the order of 1 μm, small compared to the shell wall thickness. The δ and β values used for the DVB foam were calculated based on the elemental composition and density and are listed in Table I. β is significantly higher for the DVB foam than D-T, however, the overall absorption by the foam is approximately 1%. Thus, the DVB foam shell is primarily a phase object and makes a suitable substitute for D-T.

The second surrogate capsule was chosen because of its unique surface structure. Polyimide shells on a plastic (CH) mandrel[38] have occasionally been made with a smooth outer surface and a rough inner surface. The rough inner surface is due to particular conditions during the polyimide curing process and ordinarily is very

undesirable, but ideal for this experiment. This capsule was selected to test phase contrast enhanced imaging of an object with a roughened inner surface. As shown in Table I, polyimide and CH have values of δ at 20 keV comparable to that of D-T at 8 keV. Therefore, this capsule makes a suitable surrogate when used with 20 keV x-rays.

The first surrogate capsule, denoted as the foam capsule throughout this paper, is a 1069 μm outer radius, 140 μm thick hollow DVB foam shell with a 17 μm thick solid CH over-coat. The over-coat both protects the delicate foam shell and provides a second layer to better approximate the solid D-T layer inside of a Be(Cu) shell. Ideally, a thicker CH coating would have been used, however, such a thick layer could not be produced before the experiment. The second surrogate, denoted as the polyimide capsule, is a 1087 μm outer radius 162 μm thick polyimide shell on a 13 μm thick CH mandrel. The dimensions of both surrogates were determined using a combination of optical characterization and by weighing them before and after the coating process. The shell thicknesses are known to within $\pm$ 2 μm.

Phase-contrast modeling conducted prior to the experiment confirmed that these samples would perform as reasonable surrogates for the solid D-T layer. However, it is necessary to increase the propagation distances relative to those given in Fig. 3 because of the different energies and phase shifts involved with the surrogate experiments. In the most extreme instance, propagation distances between 500 mm and 1000 mm are required for the foam surrogate used with 20 keV x-rays in order to provide reasonable phase contrast even with the plane-wave illumination, as shown in Fig. 4. When compared to Fig. 3, Δz clearly needs to be larger to achieve phase contrast comparable to a NIF baseline capsule at 8 keV. However, the essential features of phase contrast imaging are still present.

III. EXPERIMENTAL

Imaging experiments were carried out at the Advanced Photon Source (APS). The APS has the advantage of high flux from a beam with high spatial coherence. The experiments with surrogate capsules were carried out on the 1-ID undulator beam-line at the APS. A silicon (111) monochromator is used to select the x-ray energy. Measurements were made at both 10 keV and 20 keV photon energies. The bandwidth of the radiation was about 2 eV. The undulator gap was adjusted such that the usable beam size at the sample location, which is 60 m from the source, was about 2 mm x 2 mm. Since the normal odd-harmonic central cone of the undulator radiation is smaller than 2 mm at 60 m, radiation slightly off harmonic is used in order to have the larger field of view. The x-ray flux is on the order of 10^{11} photons/second, so it takes less than a second to acquire an image. Each surrogate capsule was glued onto a 1 mm diameter glass tube.
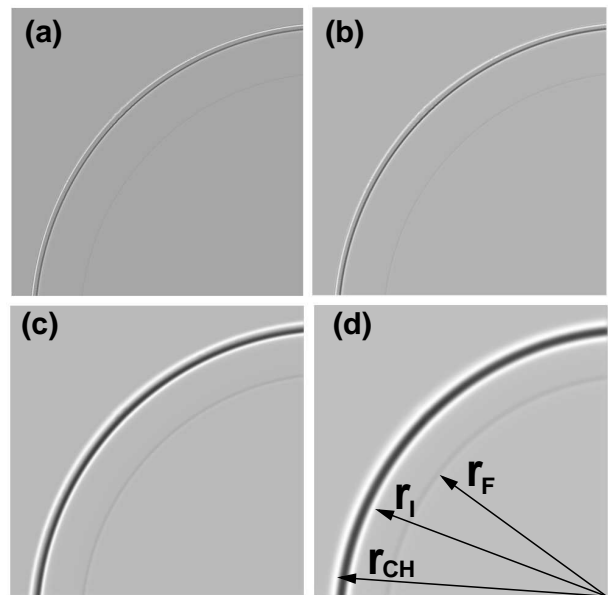

FIG. 4: Images generated using a full-wave calculation of free-space propagation of the foam capsule in the APS undulator with Δz of (a) 50 mm, (b) 100 mm, (c) 500 mm, and (d) 1000 mm. These calculations incorporated the 15 micro-radian divergence and 3 μm detector of the 1-ID undulator beam-line at the APS. The outer plastic surface (r_{CH}), inner foam surface (r_F) and the interface between the plastic and foam (r_I) are indicated in (d). Note that the inner foam boundary contrast increases with propagation distance. This is analogous to the solid D-T case illustrated in Fig. 3.

Three translational and one rotational stage enabled positioning of the capsule in the x-ray beam. The x-ray beam passed through the capsule onto a 300 μm thick CdW0$_4$ scintillator. The scintillator was optically magnified with a Mituyoyo 10x objective and imaged onto a 1024x1024 Princeton Instruments LN$_2$ cooled CCD camera.

The x-ray beam is not spatially uniform due to the radiation pattern produced by the undulator and artifacts from the beryllium windows and the monochromator. Further, the structure has a varying temporal component. Up to four images were averaged to reduce the temporal variations. The normalized image intensity I_n presented in the figures is given by

$$I_n = \frac{I - I_d}{I_0 - I_d}. \qquad (1)$$

Here, I is the CCD intensity with the capsule in the beam, I_0 is the CCD intensity with the object removed from the beam path, and I_d is the CCD dark count. I_n is known in traditional radiography as the transmission, however, that term is not applicable in this context because the phase effects cause I_n to differ from absorption imaging. The exposures were timed so that I_0 is close to the CCD saturation level. At this point, $I_0/I_d \approx 50$. The contrast between any two points is taken as the difference

of I_n at those two points.

The source size (one-sigma values) at the undulator is asymmetric, 15 μm in the vertical direction and 250 μm in the horizontal direction. The geometric blurring, given by the spot size multiplied by the ratio of the object-to-detector distance, Δz, to the source-object distance of 60 m, is much larger in the horizontal direction than the vertical. Less than 0.5 μm blurring is expected in the vertical direction, compared with up to 4.8 μm in the horizontal direction for measurements taken with the largest $\Delta z = 1156$ mm. Thus, all lineouts were taken through the image in the vertical direction to minimize the geometric blurring. There is additional blurring resulting from the scintillator and the optical imaging onto the CCD which were not characterized. However, based on comparison of the experimental images to models, the blurring has Gaussian width σ of approximately 3-5 μm.

The sample and detector are both on translation stages to enable positioning within the x-ray beam. Δz was varied between a few millimeters and over 1 meter. Images taken with the detector close to the object are nearly absorption only images, while those with increased distance show more phase-enhanced contrast at the interfaces as expected from the calculated images (Figs. 3 and 4).

A. Measurements

Four 1/4 images of the foam capsule taken with increasing Δz are shown in Fig. 5. Each image has a 1 s exposure using 20 keV x-rays and was normalized according to Eq. 1. Lineouts are shown in the left panel of Fig. 6 for each of the images. It is evident from both the images and lineouts that there is very little absorption in the foam capsule. I_n in the foam region of the image is only 1% less than that outside the capsule, and only about 1/2% smaller in the foam wall than in the hollow center region. This is compared to the 10 percent peak-to-valley contrast due to refraction at r_F for Δz of 1141 mm. The figures clearly show that the interface contrast increases steadily with increasing Δz.

The right panel of Fig. 6 shows lineouts from the same capsule using 10 keV x-rays. The contrast at 10 keV, due to the significantly higher DVB and CH δ values, is much greater at the interfaces than the 20 keV images. For Δz of 1141 mm at 20 keV and 1156 mm at 10 keV, the contrast at the inner foam surface is 0.1 and 0.43 respectively. This is in good agreement with an increase in δ by a factor of 3.9 from 20 keV to 10 keV for DVB as listed in Table I. At 10 keV, the phase enhanced contrast makes the inner foam surface clearly visible when Δz is only 156 mm. At 10 keV, δ for the DVB foam is roughly 1/3 of the value for D-T at 8 keV. Even at 20 keV, where δ is 1/10 that of solid D-T, the phase enhance contrast is easily visible in the images. This leads to one of the primary conclusions of this study which is that phase contrast enhanced imaging will enable characterization of the solid D-T surface.
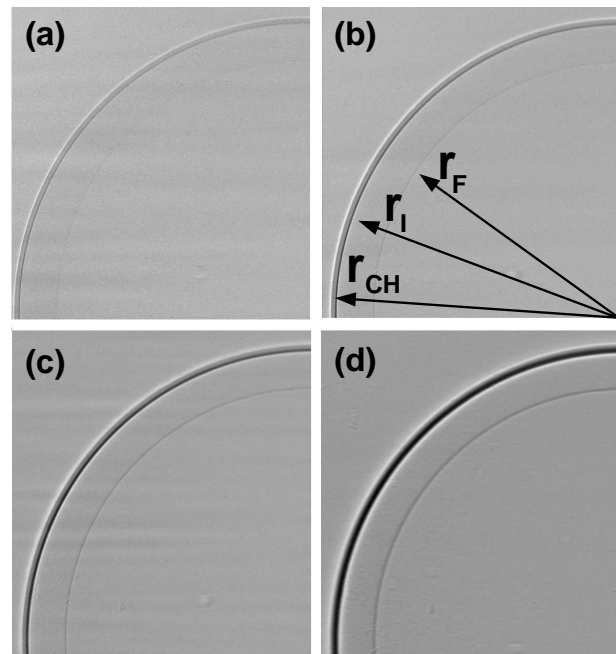

FIG. 5: Images taken at the APS using 20 keV x-rays in one second exposures of 1/4 of the foam capsule surrogate at Δz of (a) 41 mm, (b) 141 mm, (c) 441 mm, and (d) 1141 mm. The arrows in (b) mark the outer CH edge (r_{CH}), the CH-foam interface (r_I), and the inner foam surface (r_F). The interfaces are easily visible due to the phase contrast, even though the absorption contrast is much smaller.

Figure 7 shows 1/4 images of the polyimide capsule at four different Δz. The roughness on the inner CH surface of the capsule is clearly visible in the images. As with the foam capsule, the edges have enhanced contrast with increasing Δz. The two interfaces, r_I and r_{CH}, highlighted by their sharp contrast transitions, follow the thickness variations. Bumps and divots that are imaged away from the shell edge also become more visible with increased Δz. However, their contrast decreases the closer they are in the image to the center of the capsule. The contrast of the bumps and divots in Fig. 7 (d) is typically 10-12%, 6%, and 3% for $r \approx 800$ μm, 725 μm, and 640 μm, respectively. The contrast variations are less than 1% for $r < 300$ μm.

Lineouts for the images shown in Fig. 7 are given in Fig. 8. The edge contrast increases steadily with Δz for all the interfaces except at r_{CH}. There, the contrast clearly is dependent on the local roughness, especially for larger Δz. In Fig. 8 for Δz of 1141 mm, the contrast at $r = 885$ μm is lower than for Δz of 441 mm. It is clear from image (d) in Fig. 7 that I_n is higher when the defects bring the interface toward the center of the capsule and lower when the defect moves the interface away from the center of the center. The inner surface, r_{CH}, of the polyimide capsule was found by using a steepest gradient edge detection algorithm and is shown in Fig. 9 for $\Delta z = 141$ mm. The measured RMS is 1.53 μm.
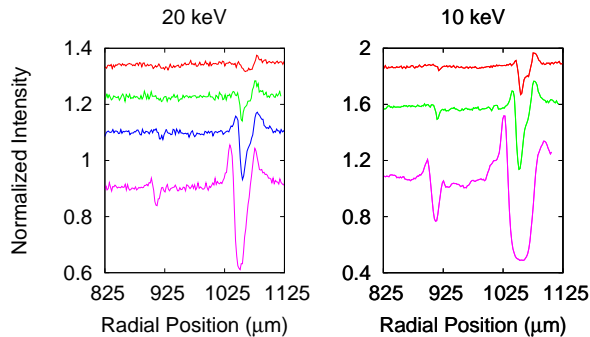
FIG. 6: Lineouts taken of the four images in Fig. 5 (left) using 20 keV x-rays and three images (not shown) using 10 keV x-rays (right). The lines are offset vertically by constant amounts for clarity. The Δz values are, from top to bottom, 41 mm, 141 mm, 441 mm, and 1141 mm (left) and 46 mm, 156 mm, and 1156 mm (right). The edges are enhanced strongly with increasing Δz. The interfaces, determined using independent characterization, are $r_{CH} = 1086$ μm, $r_I = 1069$ μm, and $r_F = 929$ μm. In each case, the plots are aligned horizontally to put the outer surface at 1086 μm.
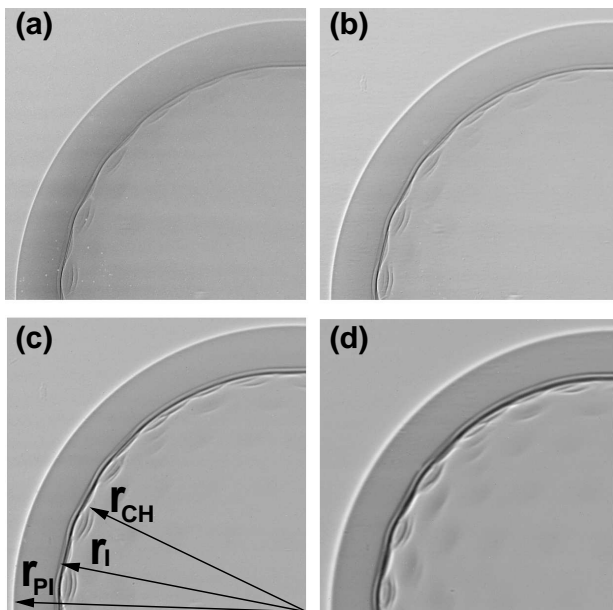

FIG. 7: Images taken at the APS using 20 keV x-rays of 1/4 of the polyimide capsule at Δz of (a) 41 mm, (b) 141 mm, (c) 441 mm, and (d) 1141 mm. The arrows in (c) point to the outer polyimide surface (r_{PI}), the polyimide-CH interface (r_I), and the inner CH surface (r_{CH}). The interfaces of are easily visible due to the phase contrast enhanced imaging, even though the absorption contrast is much smaller.

IV. COMPARISON OF EXPERIMENTS WITH MODELS

Computational models of the surrogate capsules are compared with corresponding experimental data to validate the modeling codes and understand the details of
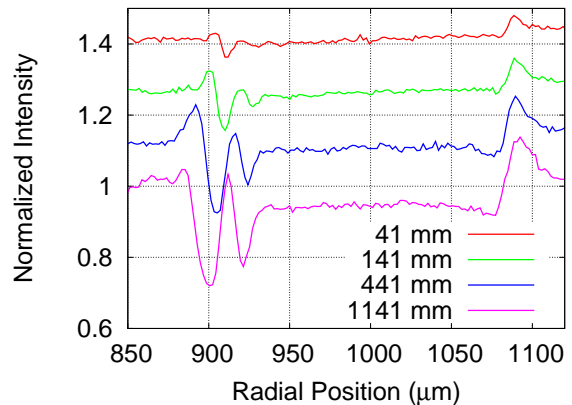

FIG. 8: Lineouts for the polyimide capsule shown in Fig. 7. The lines are offset vertically by constant amounts for clarity. The capsule interfaces, determined using independent characterization, are $r_{PI} = 1087$ μm, $r_I = 925$ μm, and $r_{CH} = 911$ μm. Each plot has been positioned so that r_{PI} is at 1087 μm. While there is little absorption of the 20 keV x-rays, the edges are enhanced with increasing Δz due to the phase-contrast.
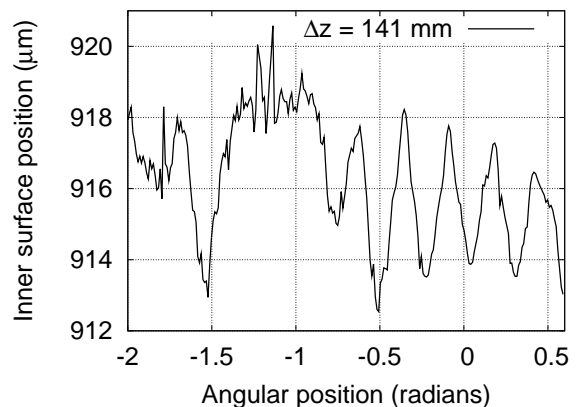

FIG. 9: Plot of the inner surface of the polyimide capsule as a function of angle for $\Delta z = 141$ mm. The surface was determined by using a steepest gradient edge detection algorithm.

phase contrast imaging. Images and lineouts are calculated using modeling of surrogate capsules and experimental conditions. The model parameters, such as capsule dimensions and system blurring, are iterated until the simulated images are consistent with the experimental data. This provides insight into both phase contrast imaging and the models and enables improved predictive capabilities.

One question of interest is the role of diffraction in phase contrast imaging of 1 mm radius capsules. The high coherence of the synchrotron radiation and the large Δz used in this experiment suggest that a full-wave model, including diffraction effects, is required. However, the full-wave calculation, used to generate Figs. 3 and 4, showed that the expected peak-to-valley separation of

the diffraction peaks was about 2 μm, or one pixel in the image, for Δz of 1150 mm. Gaussian blurring of $\sigma = 3$ μm is enough to smooth the diffraction so that it is not visible in images. This amount of blurring is consistent with the experimental data. When blurring is included, the radial profile generated using the full-wave calculation is nearly identical to the raytrace model. Thus, the image contrast is dominated by refraction and the experimental results are compared to raytraced models instead of full-wave models.

Two different raytracing software packages were used. The TracePro[39] commercial package can only model simple shapes and was used to model perfect, concentric spheres in a geometry consistent with the APS experiments. The interface contrast, apparent position, and imaging blurring can be quickly simulated using the perfect spheres. The raytracing code SHELL3D[40, 41] was used to simulate images of solid D-T in Be(Cu) ablator shells where perturbations on the innermost D-T surface are included. The D-T surface is described using spherical harmonics in SHELL3D and is significantly slower than TracePro. Both packages model refraction and absorption, but not diffraction. Gaussian blurring consistent with the experiment was applied to the simulated images.

A. TracePro models of the surrogate capsules

TracePro was used to model the foam and polyimide capsules assuming that both consist of perfect, concentric spherical surfaces. The complex refractive indices listed in Table I were used to describe the materials. A collimated beam with a 30 micro-radian divergence was used, and the detector was placed at several Δz. The wavelengths used in the model correspond to the 10 keV and 20 keV photon energies, as appropriate for the experimental conditions. However, since this is a ray-model, setting the wavelength serves only to select the wavelength dependent δ and β.

Lineouts were calculated using the 10 keV x-ray TracePro model of the foam capsule in a geometry consistent with the APS experimental data and are shown in the Fig. 10. As with the experimental data, the three interfaces are clearly distinguishable for each Δz. The model shows a consistent increase in the contrast at the interfaces with increasing Δz. Lineouts for the TracePro model of the perfectly spherical polyimide capsule are shown in Fig. 11. The model used complex refractive indices for 20 keV x-ray energy and Δz corresponding to the experiment. The radial intensity profile is very similar to the corresponding experimental data in Fig. 8.

The thin CH layer in both surrogates aids in determining the amount of blurring to apply to the system. Gaussian blurring widths were varied to match as closely as possible the shape of I_n around $r = 990$ μm in Fig. 10, and between $r = 800$ μm and $r = 875$ μm in Fig. 11. It was found that σ of 3 μm to 5 μm, depending on the
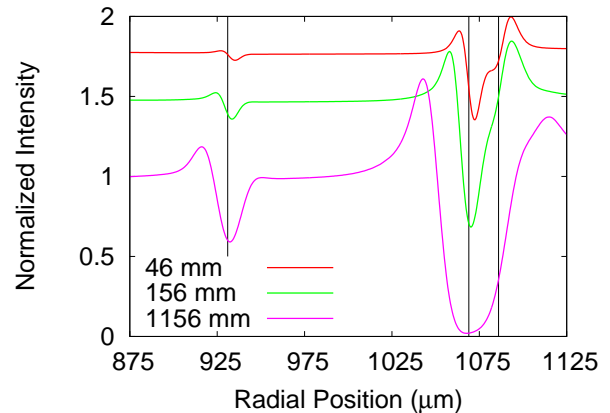

FIG. 10: Lineouts taken from TracePro model of the foam capsule with a CH over-coat at three different values of Δz. The photon energy used for modeling was 10 keV. This figure should be compared to the right panel of Fig. 6. The three lines are offset by a constant amount for clarity. The vertical lines mark the radii set in the model as $r_{CH} = 1086$ μm, $r_I = 1069$ μm, and $r_F = 929$ μm.

image, were needed to match the experimental images. The variation in σ may be the result of a change in the capsule position on the scintillator, which may not be flat with respect to the optics imaging the scintillator onto the CCD.

Interface contrast in the capsule models is significantly higher than their respective experimental data. For example, the foam capsule has contrast of 0.6 at r_{CH} in the experimental data, compared to 0.9 for the model, both at $\Delta z = 156$ mm and 10 keV. Similarly, the polyimide capsule has contrast of 0.2 at r_{PI} in the experimental data, compared to 0.6 in the model at $\Delta z = 1141$ mm. A full-wave calculation predicts the same interface contrast as the raytrace model. These differences cannot be explained consistently by using different capsule dimensions, Δz, or image blurring. Since the contrast is proportional to the material density, a decrease in the capsule densities by a factor of ≈ 2 would be required to explain the difference between experiment and model. The polyimide and CH densities are known to within 5-10%. Furthermore, the more likely density shift due to oxygen and water absorption by the polyimide and CH would increase the shell densities. At present, the difference between the experiment and model contrast cannot be explained.

Both the experimental data and simulation show a shift in the positions of the intensity peaks and valleys with increasing Δz. This is due to the very small divergence of the x-ray beam after being refracted by the shells, as is evident in Fig. 2. Moving the detector further from the shell increases the width of the interface in the image. As would be expected, the shift is much larger with increased δ, as is evident by comparing the left and right panels of Fig. 6. The models show that the outer capsule surface is marked by the steepest gradient,
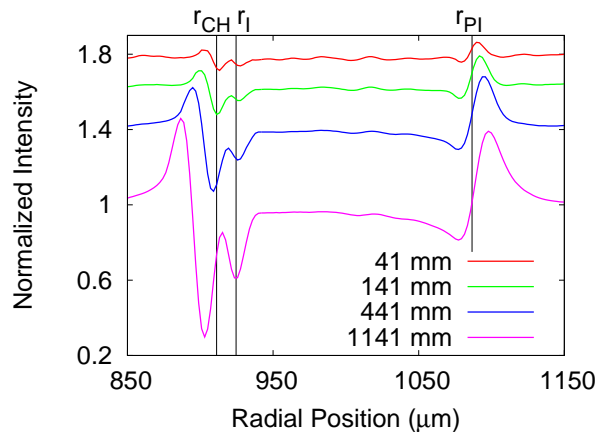
FIG. 11: Lineouts taken from TracePro model of the polyimide capsule with the detector at four Δz corresponding to the experiment. The contrast increase with Δz is obvious and shares many similarities with the data shown in Fig. 8. The interfaces are set in the model to $r_{PI} = 1086$ μm, $r_I = 925$ μm, and $r_{CH} = 911$ μm, shown by the vertical lines.

FIG. 12: Raytraced 1/4 image of a Be shell with D-T inside using complex refractive indices in Table I at 8 keV. The outer Be shell (r_{Be}), Be-DT interface (r_{Be-DT}), and the inner D-T surface (r_{DT}) are clearly visible. The inner D-T surface has 3.4 μm RMS roughness generated from spherical harmonic l and m modes 1-40.

not by the peak or minimum intensity, as demonstrated in Fig. 11. Based on this result, the steepest gradient at the outer capsule surface was referenced to identical r for each Δz. The apparent position of the inner surfaces clearly depends on Δz and the amount of refraction at the interfaces. Therefore, care must be taken in determining the interface positions, especially when Δz is large.

One noticeable difference between the model and experiment is at the r_{CH} of the polyimide capsule for Δz of 1141 mm. The model has a large increase in contrast compared to the inside of the capsule at $r = 911$ μm at that interface, whereas the data has only a small contrast increase. The difference comes from the rough experimental surface. In fact, the contrast at r_{CH} depends on the angular position of the lineout. This is clearly seen in Fig. 7 where that interface shows strong variations in contrast in relation to the bumps on the surface. A study of rough surfaces was made using SHELL3D.

B. Model of a rough surface

The roughness of the inner surface of the polyimide capsule is apparent in the experimental images. The roughness is visible as intensity variations in the image itself and angular variations in the radial position of the intensity changes. Edge detection was used to quantify the roughness of the polyimide capsule. However, an independent measurement of the polyimide capsule roughness is not available, so a direct comparison cannot be done experimentally. Instead, modeling is used to determine if phase contrast imaging can be used to accurately measure the capsule roughness.

SHELL3D, previously described for visible light applications,[40, 41] was used to model the rough sur-
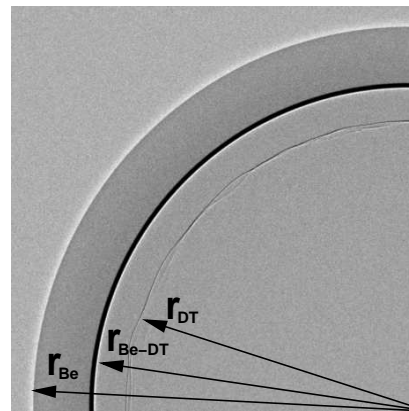
face. Briefly, simulated images are produced by raytracing through three spherical surfaces. In this case, the spherical shells are chosen as a solid D-T layer inside of a beryllium shell. The rough solid D-T surface is described by spherical harmonics. Images are generated using the x-ray wavelength and refractive index. These images are passed to a second code which locates the interfaces using a steepest gradient in image intensity.[42] The detected surface is compared with the model surface to determine how accurately the rough surface can be followed in phase contrast x-ray images.

A representative image of a rough D-T surface inside of a spherical Be(Cu) shell is shown in Fig. 12. 100 million rays were collected at a plane 100 mm from the shell to generate the images. The refractive indices used in the model are those listed in Table I for D-T and Be(Cu) at 8 keV. The radii were set to $r_{Be} = 1000$ μm, $r_{Be-DT} = 850$ μm, and $r_{DT} = 750$ μm. The inner D-T surface has an RMS roughness of 3.4 μm, clearly visible in the image.

The detected radius of the inner band from the simulated image and the model input surface for the two images are shown in Fig. 13. The model line is extracted from the 2D surface at the center of the shell defined perpendicular to the x-ray beam. The surface with 1.4 μm RMS is followed very well by the edge detection. Some deviation from the input surface is seen for the surface with 3.4 μm RMS. The roughness is large enough that features out of the center-plane begin to influence the image contrast. Such features are visible in Fig. 12 where the edge splits, and in (d) of Fig. 7 where the multiple radial intensity variations are present at each angular position. The RMS roughness extracted from the image differs by less than 1% for the 1.4 μm case, and 3% for the 3.4 μm case from the model input power. The Fourier mode analysis is also in good agreement over all

modes. Thus, following the edge in the phase-contrast enhanced images accurately reproduces the surface profile and RMS roughness.
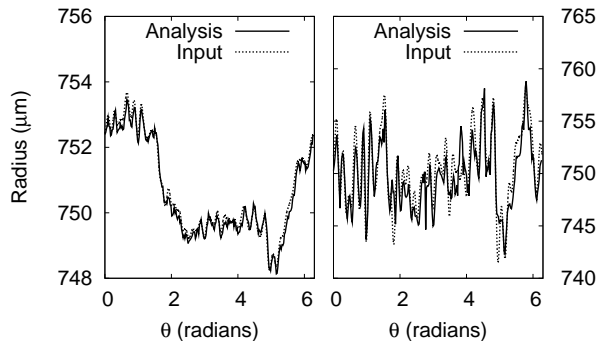

FIG. 13: Result of comparison of the edge detected surface and the model input for (left) 1.4 μm RMS and (right) 3.4 μm RMS surfaces. The lower RMS surface is followed better than the 3.4 μm surface. Spherical harmonics up to mode 40 were included in both cases. Note the different vertical scales.

V. FUTURE WORK

NIF ignition capsules will need to be characterized just before shot time which requires a laboratory based x-ray source. In the Fresnel approximation, propagation from a point source is equivalent to propagation of a plane-wave through a different distance, therefore the technique described earlier in this paper is in principle readily extensible to point projection imaging using laboratory x-ray sources. High-resolution point projection x-ray microscopes have been discussed elsewhere in the literature[31, 32, 43] and are ideal candidates for imaging the solid D-T layer.[27] Consider, for example, a 10 μm full-width-half-max (FWHM) micro-focus x-ray source illuminating the NIF baseline capsule. Let the x-ray source be located 50 mm from the NIF baseline capsule and the x-ray detector be located 50 mm downstream of the object. The magnification of the system is 2x, providing sufficient magnification for micron-scale variations in the solid D-T layer to be visible with readily available x-ray detectors.

Such characterization of NIF ignition capsules has recently been deomonstrated using a laboratory based micro-focus x-ray source.[44] Characterization of the surface roughness has been demonstrated for such layers. The models of rough surfaces presented in this article consider sums of Legendre polynomials. These surfaces are always continuous. Real surfaces may have cracks, voids, or other localized defects that are not readily described by Legendre polynomials. Furthermore, such roughness may not be accurately characterized simply by following the surface. Instead, new methods for reconstructing the surface which include both the surface position as well as the contrast at that surface require

further investigation.

A more complete reconstruction of the surface requires multiple images, possibly taken from several angles. In particular, NIF ignition experiments require capsules placed inside of a cylindrical hohlraum. The cylindrical thermal environment breaks the spherical symmetry of the D-T layers. Additional external factors, such as centering of the capsule inside of the hohlraum, will also lead to asymmetries in the layer. A single image may not capture the full 3D geometry of the capsule. A future experiment is planned to characterize a D-T layer inside of a hohlraum from several different angles.

VI. SUMMARY

The possibility of phase contrast enhanced x-ray imaging for characterization of solid D-T inside NIF beryllium ablator shells was studied. Two surrogate capsules with δ comparable to solid D-T were successfully imaged at the Advanced Photon Source. The phase contrast was rendered visible by free-space propagation. Both raytrace models and Fresnel calculations are consistent with the experimental images when the system resolution is included.

The rough surface inside of a polyimide capsule was rendered visible by phase contrast at the APS. The surface is located in the image by an edge detection algorithm. A raytrace calculation of a rough surface was shown to quantitatively reflect the rough surface using phase-contrast enhanced imaging. These results demonstrate that the solid D-T surface inside of beryllium shells can be characterized using phase-contrast enhanced x-ray imaging.

[1] S. W. Haan, S. M. Pollaine, J. D. Lindl, L. J. Suter, R. L. Berger, L. V. Powers, W. E. Alley, P. A. Amendt, J. A. Futterman, W. K. Levendahl, et al., Physics of Plasmas **2**, 2480 (1995).

[2] J. Lindl, Physics of Plasmas **2**, 3933 (1995).

[3] J. D. Lindl, P. Amendt, R. L. Berger, S. G. Glendinning, S. H. Glenzer, S. W. Haan, R. L. Kauffman, O. L. Landen, and L. J. Suter, Physics of Plasmas **11**, 339 (2004).

[4] J. D. Kilkenney, S. G. Glendinning, S. W. Haan, B. A. Hammel, J. D. Lindl, D. Munro, B. A. Remington, S. V. Weber, J. P. Knauer, and C. P. Verdon, Physics of Plasmas **1**, 1379 (1994).

[5] M. M. Marinak, S. G. Glendinning, R. J. Wallace, B. A. Remington, S. V. Weber, S. W. Haan, and G. W. Collins, Physics of Plasmas **9**, 3567 (2002).

[6] S. W. Haan, T. Dittrich, G. Strobel, S. Hatchett, D. Hinkel, M. Marinak, D. Munro, O. Jones, S. Pollaine, and L. Suter, Fusion Technology **41**, 164 (2002).

[7] R. B. Stephens, S. W. Haan, and D. C. Wilson, Fusion Technology **41**, 226 (2002).

[8] D. C. Wilson, P. A. Bradley, N. M. Hoffman, F. J. Swenson, D. P. Smitherman, R. E. Chrien, R. W. Margevicius, D. J. Thoma, L. R. Foreman, J. K. Hoffer, et al., Physics of Plasmas **5**, 1953 (1998).

[9] D. E. Hinkel, S. W. Haan, A. B. Langdon, T. R. Dittrich, C. H. Still, and M. M. Marinak, Physics of Plasmas **11**, 1128 (2004).

[10] T. J. Asaki, Fusion Technology **35**, 126 (1999).

[11] T. J. Asaki, J. K. Hoffer, and J. D. Sheliak, Fusion Technology **33**, 171 (1998).

[12] T. Hale, T. Asaki, K. Telschow, and J. Hoffer, in *SPIE-Int. Soc. Opt. Eng. Proceedings of Spie - the International Society for Optical Engineering*, edited by R. H. Bossi and D. M. Pepper (SPIE, San Antonio, TX, USA, 1998), vol. 3399, pp. 97–108.

[13] R. Fitzgerald, Physics Today **53**, 23 (2000).

[14] K. A. Nugent, T. E. Gureyev, D. F. Cookson, D. Paganin, and Z. Barnea, Phys. Rev. Lett. **77**, 2961 (1996).

[15] U. Bonse and M. Hart, Applied Physics Letters **6**, 155 (1965).

[16] K. Hirano and A. Momose, Jpn. J. Appl. Phys. **38**, L1556 (1999).

[17] K. Iwata, H. Kikuta, H. Tadano, H. Hagino, and T. Nakano, Jpn. J. Appl. Phys. **38**, 6535 (1999).

[18] A. Yoneyama, A. Momose, E. Seya, K. Hirano, T. Takeda, and Y. Itai, Rev. Sci. Instruments **70**, 4582 (1999).

[19] A. Yoneyama, A. Momose, and I. Koyama, Jpn. J. Appl. Phys. **41**, L161 (2002).

[20] V. N. Ingal and E. A. Beliaevskaya, Journal of Physics D **28**, 2314 (1995).

[21] V. A. Bushuev, E. A. Beliaevskaya, and V. N. Ingal, Il Nuovo Cimento D **19**, 513 (1997).

[22] I. Schelokov, T. Weitkamp, and A. Snigirev, Optics Communications **213**, 247 (2002).

[23] B. Yaakobi and A. J. Burek, IEEE Journal of Quantum Electronics **QE-19**, 1841 (1983).

[24] E. Forster, K. Goetz, and P. Zaumseil, Kristall und Technik **15**, 937 (1980).

[25] D. Paganin and K. A. Nugent, Phys. Rev. Lett. **80**, 2586 (1998).

[26] P. Cloetens, R. Barrett, J. Baruchel, J.-P. Guigay, and M. Schlenker, J. Phys. D **29**, 133 (1996).

[27] S. W. Wilkins, T. E. Gureyev, D. Gao, A. Pogany, and A. W. Stevenson, Nature **384**, 335 (1996).

[28] A. Snigirev, I. Snigireva, V. Kohn, S. Kuznetsov, and I. Schelokov, Rev. Sci. Inst. **66**, 5486 (1995).

[29] T. E. Gureyev, C. Raven, A. Snigirev, I. Snigireva, and S. W. Wilkins, J. Phys. D. **32**, 563 (1999).

[30] B. E. Allman, P. J. McMahon, J. B. Tiller, K. A. Nugent, D. Paganin, A. Barty, I. McNulty, S. P. Frigo, Y. Wang, and C. C. Retsch, J. Opt. Soc. Am. A **17**, 1732 (2000).

[31] A. Pogany, D. Gao, and S. W. Wilkins, Review of Scientific Instruments **68**, 2774 (1997).

[32] T. E. Gureyev and S. W. Wilkins, J. Opt. Soc. Am. A **15**, 579 (1998).

[33] D. S. Montgomery, A. Nobile, and P. J. Walsh, Review of Scientific Instruments **75** (2004).

[34] C. Logan, Y.-M. Wang, M. Aufderheide, and H. Martz, Tech. Rep. UCID-ID-145954, Lawrence Livermore National Laboratory, Livermore, CA 94550 (2001).

[35] B. L. Henke, E. M. Gullikson, and J. C. Davis, Atomic Data & Nuclear Data Tables **54**, 181 (1993), as listed at http://www.cxro.lbl.gov/optical_constants/.

[36] P. C. Souers, *Hydrogen Properties for Fusion Energy* (University of California, Berkeley, 1986).

[37] J. Streitt and D. Schroen, Fusion Science and Technology **43**, 321 (2003).

[38] S. A. Letts, A. E. H. Nissen, P. J. Orthion, S. R. Buckley, E. Fearon, C. Chancellor, C. C. Roberts, B. K. Parrish, and R. C. Cook, Fusion Technology **41**, 268 (2002).

[39] Raytracing was performed using the TracePro^{TM} commercial optical modeling program. For further information contact Lambda Research Corp., Littleton, MA 01460.

[40] J. A. Koch, T. P. Bernat, G. W. Collins, B. A. Hammel, B. J. Kozioziemski, A. J. MacKinnon, J. D. Sater, D. N. Bittner, and Y. Lee, Fusion Technology **38**, 123 (2000).

[41] J. A. Koch, T. P. Bernat, G. W. Collins, B. A. Hammel, J. D. Sater, and D. N. Bittner, Fusion Science and Technology **43**, 55 (2003).

[42] E. R. Mapoles, J. Sater, J. Pipes, and E. Monsler, Phys. Rev. E **55**, 3473 (1997).

[43] S. Wang, F. Duewer, S. Kamath, C. Kelly, A. Lyon, K. Nill, D. Scott, D. Trapp, Y. Wenbing, S. Neogi, et al., in *Proceedings of the 28th International Symposium for Testing and Failure Analysis* (Phoenix, AZ, USA, 2002), pp. 227–233.

[44] B. J. Kozioziemski, J. D. Sater, J. D. Moody, J. J. Sanchez, R. A. London, A. Barty, H. E. Martz, and D. S. Montgomery, Journal of Applied Physics **98**, 103105 (2005).